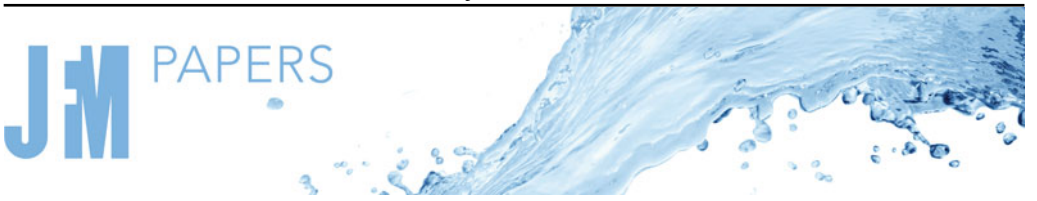
*J. Fluid Mech.* (2025), *vol.* 1013, A35, doi:10.1017/jfm.2025.10265




# Pattern formation on an ice surface

**Zhihua Wang**[1], **Kwing-So Choi**[1], **Shuguang Li**[1], **Chao Sun**[2] and **Xuerui Mao**[3,4]

[1]Faculty of Engineering, University of Nottingham, Nottingham NG7 2RD, UK

[2]Department of Engineering Mechanics, School of Aerospace Engineering, Tsinghua University, Beijing 100084, PR China

[3]Beijing Institute of Technology (Zhuhai), Zhuhai 519087, PR China

[4]School of Interdisciplinary Science, Beijing Institute of Technology, Beijing 100081, PR China

**Corresponding author:** Xuerui Mao, maoxuerui@sina.com

(Received 11 December 2024; revised 11 May 2025; accepted 15 May 2025)

A linear stability model based on a phase-field method is established to study the formation of ripples on the ice surface. The pattern on horizontal ice surfaces, e.g. glaciers and frozen lakes, is found to be originating from a gravity-driven instability by studying ice–water–air flows with a range of water and ice thicknesses. Contrary to gravity, surface tension and viscosity act to suppress the instability. The results demonstrate that a larger value of either water thickness or ice thickness corresponds to a longer dominant wavelength of the pattern, and a favourable wavelength of 90 mm is predicted, in agreement with observations from nature. Furthermore, the profiles of the most unstable perturbations are found to be with two peaks at the ice–water and water–air interfaces whose ratio decreases exponentially with the water thickness and wavenumber.

**Key words:** multiphase flow, pattern formation, morphological instability

## 1. Introduction

Morphological patterns on the interface in multi-phase flows are ubiquitous in nature, such as the ripples on the surface of icicles (Ogawa & Furukawa 2002), wave-like structures on glaciers (Camporeale & Ridolfi 2012*b*), crenulations on stalactites (Camporeale & Ridolfi 2012*a*), dimples over a bed of sand below shallow wavy water (Lundbek Hansen *et al.* 2001; Charru, Andreotti & Claudin 2013), scallops on the side of icebergs (Bushuk *et al.* 2019), and patterns on lava flows (McDonald *et al.* 2022). Among them, the ripples formed on the ice surface, e.g. patterns on icicles, glaciers (see figure 1*a*), icy rivers and frozen lakes (see figure 1*b*), are related to perturbation growth in phase-change processes. These patterns change the surface roughness, which has been reported to be in strong

© The Author(s), 2025. Published by Cambridge University Press.



https://doi.org/10.1017/jfm.2025.10265 Published online by Cambridge University Press

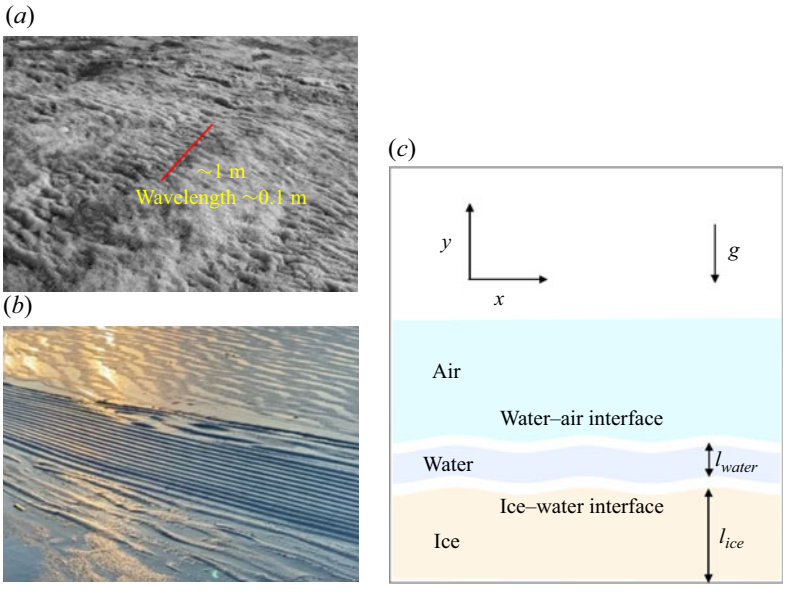



Figure 1. Examples of ice patterns. (*a*) Ice ripples on the surface of the Ciardoney glacier (North Italy, 45°31′N, 7°23′E) (Camporeale & Ridolfi 2012*b*). (*b*) An example of ice ripples on a lake (see the original figure on the website http://lakeice.squarespace.com/ice-ripples/). (*c*) Schematic view of patterns in ice–water–air flow.

correlation with the melt rates, e.g. in ice shelves (Watkins, Bassis & Thouless 2021). Investigating these pattern formations is critical to unveil the underpinning mechanism, and is of tremendous interest in developing anti-icing and de-icing devices for applications (Zhang *et al.* 2022*a*).

Efforts have been devoted to investigating the structure of ice, as well as its growth mechanisms (Murata, Nagashima & Sazaki 2019; Wang *et al.* 2021; Grivet *et al.* 2022). It has been well demonstrated that the growth of an icicle is complicated and sensitive to atmospheric conditions and the water flux (Makkonen 1988), highlighting the importance of the water and air dynamics in the consolidation process. Zwally *et al.* (2005), Rignot & Kanagaratnam (2006) and Kaser *et al.* (2006) studied the evolution of the glaciers in Greenland and the Antarctic, and reported that they can be recognised as structures of ice surrounded by water films since the ice is exposed to meltwater (Camporeale & Ridolfi 2012*b*), indicating the presence of a three-phase system with water sandwiched by ice and air (see figure 1*c*). The evolution of ice on rivers, lakes and ponds has also been studied in previous works (Leppäranta 2010; Popović *et al.* 2018; Blackburn & She 2019).

Despite these quantitative studies on the basic structures and the growth of ice, not much attention has been focused on the mechanism of the ripple formation on the ice surfaces. An axisymmetry-breaking instability in the natural convection of water within a vertical cylinder was studied numerically and experimentally. The study showed that a cold metallic surface at the top of the cylinder froze the water, and the ice front grew downwards, exhibiting high-azimuthal-wavenumber patterns in the ice–water flow (Gelfgat *et al.* 1999). A theoretical model based on hydrodynamic stability was proposed to attribute the patterns on the icicles to the growth of infinitesimal perturbations, and the wavelength of the ripples was found to be approximately 1 cm (Ogawa & Furukawa 2002). Subsequently, linear stability analysis was carried out to interpret icicle ripples, and the influence of ambient air and water on the growth of the ice–water interface disturbance was modelled separately (Ueno 2003, 2004, 2007; Ueno & Farzaneh 2011). These theoretical



https://doi.org/10.1017/jfm.2025.10265 Published online by Cambridge University Press

and numerical results were validated by comparing the wavelengths against experimental ones (Ueno *et al.* 2009). However, there is a lack of the influence of the ice layer and water layer thicknesses on the formation of patterns, although it is generally known that different thicknesses lead to distinct ripples in nature (see figure 1*b*).

Compared with the limited research on the ripples of icicles, studies on the mechanism of ice ripple formation on glaciers and lakes, where the gravity is not parallel to the interface as in the icicle scenarios, and different mechanisms can be expected, are even rarer. Among them, a mathematical model based on the well-known Orr–Sommerfeld equations was developed by treating the problem as the morphological instability of a melting–freezing interface bounding a free-surface laminar flow (Camporeale & Ridolfi 2012*b*). However, the role of the air dynamics was not accounted for, only ice and water were considered in this model, and the detailed distribution of perturbations, which is demonstrated to be focused on both the ice–water and water–air interfaces in this paper, was absent.

Another potential theory to explain the mechanism of ripple formation on a horizontal ice surface is the Rayleigh–Taylor (R–T) instability, as the heavier phase (water) is placed above the lighter one (ice) and is accelerated by gravity (see figure 1*c*). The R–T instability in two-layer flows has been studied extensively since the pioneering work of Rayleigh (1882) and Taylor (1950). However, studies on R–T instability in three-layer or multi-layer flows are comparatively limited. Mikaelian (1982) proposed a linear theory to investigate R–T instability at the interfaces of multiple stratified fluids with arbitrary density profiles, assuming that the flows are incompressible and inviscid. Parhi & Nath (1991) developed a formulation for R–T instability in three-layer incompressible and viscous flows. Jacobs & Dalziel (2005) conducted experimental investigations on R–T instability in three-layer fluids, with one unstable and one stable interface, and examined the influence of the density difference between the top and bottom layers. More recently, Adkins *et al.* (2017) used a fluid magnetic levitation technique to experimentally study R–T instability in three-layer flows with a low–high–low density distribution. Their results showed that the growth rate decreases as the height of the middle layer increases. Following this, the influences of cylindrical geometry (Guo *et al.* 2017), non-uniform velocity shear (Matsuoka 2020), strong isothermal stratification (Aslangil & Wong 2023) and nonlinear dynamics (Sengupta, Ulloa & Joshi 2023) on R–T instability in three-layer flows have been explored successively. However, limited efforts have been devoted to the effects of the thicknesses of different layers, which are critical to the icing problem studied in this work. Furthermore, existing research on the R–T instability is mainly on the interface of fluid phases, and there has been no study on the role of the R–T instability on the ripple formation around the ice surface, where heavier fluid is above lighter solid.

The purpose of this work is to investigate the mechanisms of the morphological patterns on the ice surface of glaciers and lakes with a shallow film of air-surrounded water flows, as well as the influence of the ice and water thicknesses. To study the icing process and ripple formation in such a three-phase flow, how to capture the interfaces between different phases is one of the key issues. In the mid-20th century, the idea of a non-zero thickness interface was developed, and the phase-field method was proposed (Cahn & Hilliard 1958). This method circumvents the imposition of boundary conditions on the interface by introducing additional variables that are continuous in the domain so that the physical variables do not exhibit mutations at the interface (Mirjalili, Ivey & Mani 2019). Taking this advantage, this method was then applied in the simulation of multi-phase flows such as solidification (Sabouri-Ghomi, Provatas & Grant 2001), melting (Weady *et al.* 2022), boiling (Badillo 2012) and sublimation (Reitzle *et al.* 2019), to name a few. In spite of these successful applications, there is a lack of modelling of ice ripples based



https://doi.org/10.1017/jfm.2025.10265 Published online by Cambridge University Press

on the phase-field method. Therefore, we establish a theoretical model for ice–water–air flows with phase change. The linear stability analysis is then carried out to study the morphological instability of the flows and subsequently examine the natural ice pattern growth. We find that the patterns on the ice surfaces are formed by the growth of the perturbations, which are generated on the ice–water interface, owing to an instability analogous to the gravity-driven R–T form generally found on the interface of two fluids, and propagate to the water–air interface. We note that the linear stability theory applied in this work predicts the most unstable wavelength of interface instabilities marking the formation of ripples, whilst the saturated magnitude of ripples and three-dimensional developments requiring nonlinear calculations are out of the scope of this work.

## 2. Governing equations

### 2.1. *Phase-field model for three-phase flows*

As shown in figures 1(*a*) and 1(*b*), a thin layer of meltwater is commonly anticipated to be present above the ice layer. The water, surrounded by the ambient air, has complex interactions with ice and air, which are characterised by the ice–water and water–air interfaces, respectively. For such a configuration, a two-dimensional study, as depicted in figure 1(*c*), is sufficient. The $x$ direction is parallel to the unperturbed interface, and $y$ is normal to it. Two phase-field order parameters, $\phi$ and $c$, are employed to mark the three phases and subsequently the interfaces: $\phi \in [-1, 1]$ is used to distinguish air ($\phi = -1$) from water ($\phi = 1$), while $c \in [-1, 0]$ is employed to separate water ($c = 0$) from ice ($c = -1$). The volume fractions of the air, water and ice phases in the proposed model are obtained as $\beta_g = (1-\phi)/2$, $\beta_l = (1+\phi)(1+c)/2$, $\beta_s = (1+\phi)(-c)/2$, where $\beta_g + \beta_l + \beta_s = 1$ is always true in the whole domain. Based on the volume fractions of the phases, density, viscosity, thermal conductivity and specific heat capacity are obtained by linear interpolations:

$$\begin{aligned} \rho(c,\phi) &= \beta_g \rho_g + \beta_l \rho_l + \beta_s \rho_s, \\ \mu(c,\phi) &= \beta_g \mu_g + \beta_l \mu_l + \beta_s \mu_s, \\ \kappa(c,\phi) &= \beta_g \kappa_g + \beta_l \kappa_l + \beta_s \kappa_s, \\ c_p(c,\phi) &= \beta_g c_{pg} + \beta_l c_{pl} + \beta_s c_{ps}, \end{aligned} \tag{2.1}$$

where $\rho$ is the density, $\mu$ is the viscosity, $\kappa$ is the thermal conductivity, $c_p$ is the specific heat capacity, and the subscripts $g$, $l$ and $s$ represent pure air, pure water and pure ice, respectively.

The Allen–Cahn equation (Allen & Cahn 1979) is used to model the phase change from water to ice:

$$\frac{\partial c}{\partial t} + \boldsymbol{\nabla} \cdot (\boldsymbol{u} c) = M_c \left[ 6\sigma_c \xi_c \, \boldsymbol{\nabla}^2 c - \frac{\partial f(c)}{\partial c} \right], \tag{2.2}$$

where $\boldsymbol{u}$ denotes the velocity vector, $t$ is time, $M_c$ is the phenomenological mobility, whose larger value speeds up the phase-changing process (Zhang *et al.* 2022*b*), $\sigma_c$ and $\xi_c$ denote the surface tension and the thickness coefficient of the ice–water interface, respectively. Here, $f(c) = 3(\sigma_c/\xi_c)\, g(c) + L(T_M - T)\, h(c)/T_M$ is the free energy density, where $g(c) = (c+1)^2 c^2$, $h'(c) = 30\, g(c)$, $L$ is the latent heat of fusion per unit volume, $T$ is the temperature, and $T_M$ is the melting point of ice (Boettinger *et al.* 2002; Zhang *et al.* 2022*b*).



https://doi.org/10.1017/jfm.2025.10265 Published online by Cambridge University Press

The Cahn–Hilliard equation (Cahn & Hilliard 1958) is employed to model the evolution of the interface between water and air:

$$\frac{\partial \phi}{\partial t} + \boldsymbol{u} \cdot \nabla \phi = M_\phi \, \nabla^2 \mu_\phi, \tag{2.3}$$

where $M_\phi$ is the phenomenological mobility, and $\mu_\phi$ is the chemical potential obtained from (Boettinger *et al.* 2002; Zhang *et al.* 2022*b*; Wang *et al.* 2024)

$$\mu_\phi = -\frac{3\sigma_\phi}{2\sqrt{2}} \left[ \xi_\phi \, \nabla^2 \phi - \frac{1}{\xi_\phi} (\phi^3 - \phi) \right], \tag{2.4}$$

where $\sigma_\phi$ and $\xi_\phi$ denote the surface tension and the thickness coefficient of the water–air interface, respectively.

The continuity, momentum and energy equations for the multi-phase flow are

$$\frac{\partial \rho}{\partial t} + \nabla \cdot (\rho \boldsymbol{u}) = 0, \tag{2.5}$$

$$\frac{\partial (\rho \boldsymbol{u})}{\partial t} + \nabla \cdot (\rho \boldsymbol{u} \otimes \boldsymbol{u}) = -\nabla p + \nabla \cdot \boldsymbol{\tau} + \boldsymbol{F}_b, \tag{2.6}$$

$$\frac{\partial (\rho c_p T)}{\partial t} + \nabla \cdot (\rho c_p T \boldsymbol{u}) = \frac{\partial \beta_s}{\partial t} L + \nabla \cdot (\kappa \nabla T) + \Phi + \boldsymbol{u} \cdot \boldsymbol{F}_b, \tag{2.7}$$

where $\otimes$ represents the outer product, $p$ denotes pressure, $\boldsymbol{\tau} = -2/3\mu \nabla \cdot \boldsymbol{u} \boldsymbol{I} + \mu[\nabla \boldsymbol{u} + (\nabla \boldsymbol{u})^{\mathrm{T}}] + \boldsymbol{\tau}_e$ is the total stress tensor, with $\boldsymbol{I}$ the unit diagonal tensor, superscript T indicating the transpose of a matrix, and $\boldsymbol{\tau}_e = -(3/2\sqrt{2})\sigma_c \xi_c \, \nabla c \otimes \nabla c - (3/2\sqrt{2})\sigma_\phi \xi_\phi \, \nabla \phi \otimes \nabla \phi$ being the extra elastic stress induced by the interfacial surface tension (Liu & Shen 2003; Shen 2011). Also, $\boldsymbol{F}_b = \rho \boldsymbol{g}$ is the body force, with $\boldsymbol{g}$ denoting the gravitational acceleration, and $\Phi$ is the viscous dissipation rate. The first term on the right-hand side of the energy equation (2.7) describes the latent heat due to phase change in the icing process. Note that although the fluid flow (water and air) is considered incompressible in this work, the use of a compressible form of the equations is more rigorous in phase-field models, as properties such as density and viscosity vary continuously from phase to phase around the interfaces (see (2.1)) (Kim 2012).

### 2.2. *Linear stability equations*

To study the dynamics of small perturbations, whose growth leads to the development of patterns on the ice surface, the flow field is decomposed into a base flow and a small perturbation:

$$\boldsymbol{q} = \boldsymbol{q}_0 + \boldsymbol{q}', \tag{2.8}$$

where $\boldsymbol{q} = [\boldsymbol{u}, p, c, \phi, \mu_\phi, T]^{\mathrm{T}}$ denotes the flow variables, $\boldsymbol{q}_0 = [\boldsymbol{u}_0, p_0, c_0, \phi_0, \mu_{\phi 0}, T_0]^{\mathrm{T}}$ is the steady base flow satisfying the governing equations (2.2)–(2.7) and varying in the $y$ direction only, and $\boldsymbol{q}' = [\boldsymbol{u}', p', c', \phi', \mu_\phi', T']^{\mathrm{T}}$ is the perturbation that can be further decomposed in $x$ and $t$, and each term reads

$$\boldsymbol{q}'(x, y, t) = \hat{\boldsymbol{q}}(y) \exp(\mathrm{i}\alpha x - \mathrm{i}\omega t), \tag{2.9}$$

where $\hat{\boldsymbol{q}}$ is the amplitude of the perturbation, and $\alpha$ denotes the wavenumber. Here, $\omega = \omega_r + i\omega_i$ is a complex value (with i the imaginary unit), with $\omega_r$ and $\omega_i$ representing the angular frequency and the growth rate of the perturbation, respectively. By substituting (2.8) into (2.2)–(2.7), subtracting the base flow terms, and neglecting the nonlinear terms



https://doi.org/10.1017/jfm.2025.10265 Published online by Cambridge University Press

of perturbations, the linear stability equations for the perturbations can be obtained:

$$\boldsymbol{\Gamma}\frac{\partial \boldsymbol{q}'}{\partial t}+\boldsymbol{H}_x\frac{\partial \boldsymbol{q}'}{\partial x}+\boldsymbol{H}_y\frac{\partial \boldsymbol{q}'}{\partial y}+\boldsymbol{H}\boldsymbol{q}'+\boldsymbol{H}_{xx}\frac{\partial^2 \boldsymbol{q}'}{\partial x^2}+\boldsymbol{H}_{yy}\frac{\partial^2 \boldsymbol{q}'}{\partial y^2}+\boldsymbol{H}_{xy}\frac{\partial^2 \boldsymbol{q}'}{\partial x\,\partial y}=0, \quad (2.10)$$

where matrices $\boldsymbol{\Gamma}$, $\boldsymbol{H}_x$, $\boldsymbol{H}_y$, $\boldsymbol{H}$, $\boldsymbol{H}_{xx}$, $\boldsymbol{H}_{yy}$ and $\boldsymbol{H}_{xy}$ are functions of the base flow quantities (see Appendix A for details).

The boundary conditions of the perturbations on the lower boundary (assumed as pure ice) are

$$\boldsymbol{u}'=0, \quad \frac{\partial p'}{\partial y}=0, \quad c'=0, \quad \phi'=0, \quad \mu'_\phi=0, \quad T'=0, \quad (2.11)$$

where $\boldsymbol{u}'=0$ ensures a no-slip condition, while $\partial p'/\partial y=0$ maintains pressure continuity across the solid boundary. Other perturbations are set to zero, assuming no fluctuations at the ice boundary.

The boundary conditions of the perturbations on the upper boundary (assumed as pure air) are

$$\frac{\partial \boldsymbol{u}'}{\partial y}=0, \quad p'=0, \quad c'=0, \quad \phi'=0, \quad \mu'_\phi=0, \quad T'=0, \quad (2.12)$$

where $\partial \boldsymbol{u}'/\partial y=0$ represents a stress-free condition, and $p'=0$ reflects the constant atmospheric pressure. Other perturbations are set to zero.

Substituting (2.9) into (2.10) results in

$$(-i\omega\boldsymbol{\Gamma}+i\alpha\boldsymbol{H}_x+\boldsymbol{H}_y\mathrm{D}+\boldsymbol{H}-\alpha^2\boldsymbol{H}_{xx}+\boldsymbol{H}_{yy}\mathrm{D}^2+i\alpha\boldsymbol{H}_{xy}\mathrm{D})\hat{\boldsymbol{q}}=0, \quad (2.13)$$

where $\mathrm{D}=\mathrm{d}/\mathrm{d}y$ represents the derivative with respect to $y$. Equation (2.13) is solved as an eigenvalue problem:

$$\boldsymbol{\Lambda}\hat{\boldsymbol{q}}=\omega\boldsymbol{\Gamma}\hat{\boldsymbol{q}}, \quad (2.14)$$

where $\boldsymbol{\Lambda}=\alpha\boldsymbol{H}_x-i\boldsymbol{H}_yD-i\boldsymbol{H}+i\alpha^2\boldsymbol{H}_{xx}-i\boldsymbol{H}_{yy}D^2+\alpha\boldsymbol{H}_{xy}D$.

In this paper, the temporal problem is considered, with wavenumber $\alpha$ prescribed and $\omega$ solved as the eigenvalues. The eigenvalue with the largest imaginary part, denoted as $\omega_i^{max}$, which is the growth rate of the most unstable perturbation, will be the focal of the following discussions.

A second-order finite difference method is applied, and the domain is divided equally into $N$ grids, allowing (2.14) to be solved numerically as a discretised generalised eigenvalue problem using the QR algorithm in MATLAB.

## 3. Base flow

For the configuration shown in figure 1, to ensure the coexistence of ice and water, the temperature of the base flow throughout the entire field is uniformly set to 273.15 K. It suffices here to focus on cases with zero base flow velocity, corresponding to a still lake or glacier. In this scenario, the horizontal plane perpendicular to the $y$ direction is isotropic, and the system exhibits no preferred instability direction on that plane, leading to an essentially two-dimensional formula of the instability. Therefore, as shown in (2.9), two-dimensional instabilities are considered in our work.

The lower boundary is set as pure ice ($c_0=-1$, $\phi_0=1$), and the upper boundary is treated as pure air ($c_0=0$, $\phi_0=-1$). The boundary conditions of the base flow on the lower boundary are



https://doi.org/10.1017/jfm.2025.10265 Published online by Cambridge University Press

| Phase | Density $\mathrm{kg\,m^{-3}}$ | Viscosity $\mathrm{Pa\cdot s}$ | Thermal conductivity $\mathrm{W/(m\cdot K)}$ | Specific heat capacity $\mathrm{J/(kg\cdot K)}$ |
|---|---|---|---|---|
| Air | 1.2 | $1.6\times10^{-5}$ | 0.0209 | 1003 |
| Water | 998 | $1\times10^{-3}$ | 0.5918 | 4200 |
| Ice | 898 | $1\times10^{2}$ | 2.25 | 2018 |

Table 1. Properties of air, water and ice.

| Parameter | Value | Unit |
|---|---|---|
| $M_c$ | $2.0\times10^{-5}$ | $\mathrm{m^2/(N\cdot s)}$ |
| $\sigma_c$ | $3.17\times10^{-2}$ | $\mathrm{N\,m^{-1}}$ |
| $\xi_c$ | $8.0\times10^{-5}$ | m |
| $M_\phi$ | $5.0\times10^{-10}$ | $\mathrm{m^4/(N\cdot s)}$ |
| $\sigma_\phi$ | $7.27\times10^{-2}$ | $\mathrm{N\,m^{-1}}$ |
| $\xi_\phi$ | $8.0\times10^{-5}$ | m |
| $T_M$ | 273.15 | K |
| $L$ | $3.34\times10^{8}$ | $\mathrm{J\,m^{-3}}$ |

Table 2. Values of physical parameters.

$$\boldsymbol{u}_0=0,\quad \frac{\partial p_0}{\partial y}=0,\quad c_0=-1,\quad \phi_0=1,\quad \mu_{\phi 0}=0,\quad T_0=T_M, \tag{3.1}$$

and those on the upper surface are

$$\frac{\partial \boldsymbol{u}_0}{\partial y}=0,\quad p_0=p_a,\quad c_0=0,\quad \phi_0=-1,\quad \mu_{\phi 0}=0,\quad T_0=T_M, \tag{3.2}$$

where $p_a=101\,325$ Pa is the environment pressure, and $T_M=273.15$ K represents the melting point of ice.

The values for the material properties of pure ice, water and air, and the other physical parameters, are shown in table 1 and table 2, respectively (Zhang *et al.* 2022*b*). Note that the surface tension at the ice–water interface ($\sigma_c$) is set to $3.17\times10^{-2}$ N m$^{-1}$ according to an experimental study (Hillig 1998).

Here we give an example of the motionless base flow. The steady solutions of the Allen–Cahn and Cahn–Hilliard equations (see (2.2) and (2.3)) are in the form of hyperbolic tangent type functions (Dadvand *et al.* 2021):

$$c_0(y)=-\frac{1}{2}+\frac{1}{2}\tanh\left(\frac{y-H_1}{2\xi_c}\right), \tag{3.3}$$

$$\phi_0(y)=-\tanh\left(\frac{y-H_2}{\sqrt{2}\,\xi_\phi}\right), \tag{3.4}$$

where $H_1$ and $H_2$ are arbitrary constants, whose variation produces a collection of solutions for $c_0$ and $\phi_0$ denoting the positions of ice–water and water–air interfaces. Figure 2 exhibits an example of the solutions for $c_0$ and $\phi_0$, where the domain is divided into five regions (ice layer, ice–water interface, water layer, water–air interface, and air layer) along the $y$ direction by these order parameters. The other properties of the base flow, i.e. $\gamma_0=(\rho_0,\mu_0,\kappa_0,c_{p0})$, are calculated by linear interpolation:



https://doi.org/10.1017/jfm.2025.10265 Published online by Cambridge University Press

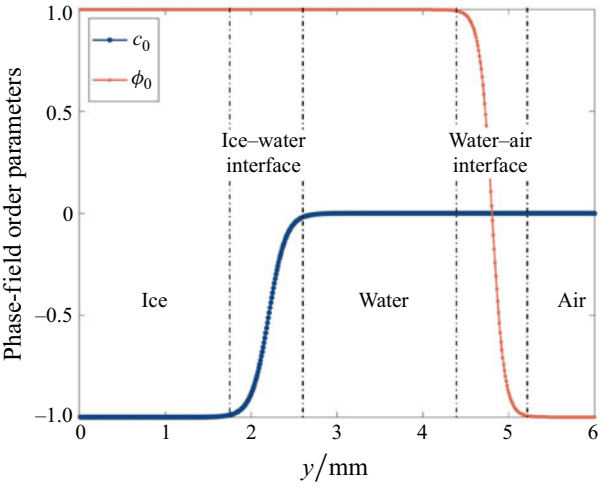



Figure 2. A distribution of phase-field order parameters $c_0$ and $\phi_0$ in the base flow.

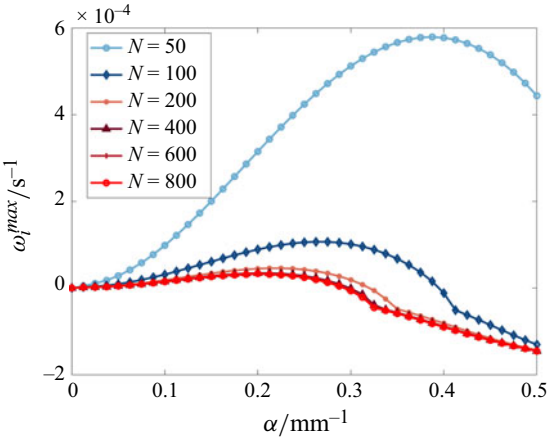



Figure 3. Dispersion relation of growth rate $\omega_i^{max}$ with wavenumber $\alpha$ for different grid numbers with $l_{ice} = l_{water} = 2$ mm.

$\gamma_0 = \beta_{g0}\gamma_g + \beta_{l0}\gamma_l + \beta_{s0}\gamma_s$, where the volume fractions $\beta_{g0}$, $\beta_{l0}$, $\beta_{s0}$ are obtained from $c_0$ and $\phi_0$ (see (2.1)).

## 4. Sensitivity studies

We first conduct a grid independence study. Figure 3 shows the dispersion relation of the growth rate $\omega_i^{max}$ with wavenumber $\alpha$ at different numbers of grid points $N$, with both the ice layer thickness $l_{ice}$ and the water layer thickness $l_{water}$ set to 2 mm. The results demonstrate that $N = 600$ is sufficient for convergence (with relative errors less than 1 % compared to $N = 800$), and this value is therefore adopted in this work.

We then conduct sensitivity studies of the mobility coefficients $M_c$ and $M_\phi$ as they are parameters required in the phase-field method. On the one hand, mobility coefficients $M_c$ and $M_\phi$ should be kept small so that the interface position is primarily advected, and on the other hand, they should be large enough to ensure that the profiles of the interface are modelled accurately (Dadvand *et al.* 2021).



https://doi.org/10.1017/jfm.2025.10265 Published online by Cambridge University Press

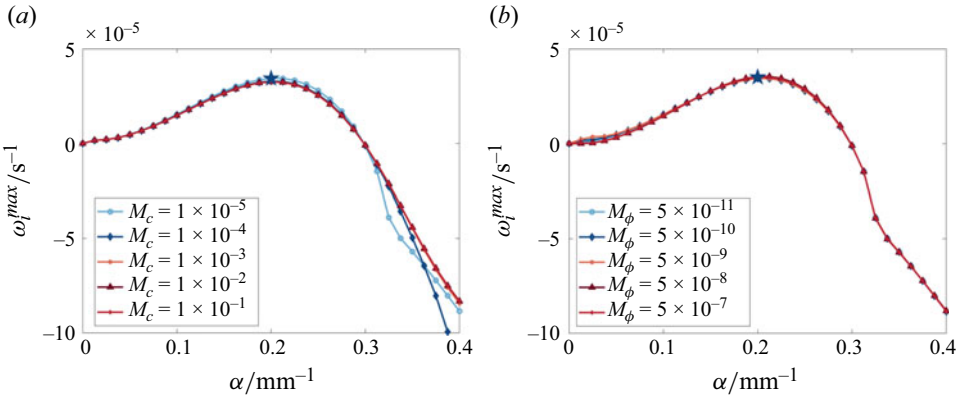



Figure 4. Dispersion relation of growth rate $\omega_i^{max}$ with wavenumber $\alpha$ for mobility coefficients (*a*) $M_c$ ($M_\phi = 5 \times 10^{-10}$), (*b*) $M_\phi$ ($M_c = 2 \times 10^{-5}$), with $l_{ice} = l_{water} = 2$ mm.

Figures 4(*a*) and 4(*b*) show the dispersion relations at different mobility coefficients, with both the ice layer thickness $l_{ice}$ and water layer thickness $l_{water}$ set to 2 mm. A wide range of values has been selected, i.e. $M_c \in [1 \times 10^{-5}, 1 \times 10^{-1}]$ and $M_\phi \in [5 \times 10^{-11}, 5 \times 10^{-7}]$. With the increase of wavenumber, the growth rate first increases from zero and then decreases to negative values, indicating that the system changes from neutrally stable to unstable and then back to stable states, illustrating a dominant wavenumber $\alpha_{dom}$, at which the growth rate maximises. We note that $\alpha_{dom}$ is the main focus of the present work, marked as blue stars in the figures since it is the wavenumber that the ice ripples are most likely to exhibit and therefore to be observed in physical experiments. The results demonstrate that $M_c$ and $M_\phi$ do not have a significant influence on the dominant wavenumber, though $M_c$ can slightly affect the absolute value of growth rates for larger wavenumbers. Overall, the values of the mobility coefficients do not have a noticeable influence on our main results. In the following, $M_c = 2 \times 10^{-5}$ and $M_\phi = 5 \times 10^{-10}$ are adopted according to Zhang *et al.* (2022*b*), Shen & Yang (2009), Dadvand *et al.* (2021) and Sato & Koshimura (2023).

## 5. Validation

Our method is validated by computing the wavelength of ripples on the icicles and comparing it against experimental results available in Ueno *et al.* (2009). The ripple formation on icicles is selected for validation because it shares similar physical processes and mathematical models with ripple formation on glaciers or lakes studied in this paper, and there are available experimental data to benchmark our results.

Figure 5(*a*) shows the velocity profiles of the base flows at $qpl = 0.0056{-}0.0278$ cm$^2$ s$^{-1}$, with $qpl$ denoting the water flow rate per width on the icicle surface. The layer with zero velocity denotes the ice layer ($y < 0.02$ cm), while the domain with velocity increasing is the water layer. Refer to Ueno *et al.* (2009) for the relationship between the velocity profile and the water supply rate. It can be seen in the figure that a larger water supply rate corresponds to a larger water layer thickness and a larger velocity of the water flow, matching the results in Ueno *et al.* (2009).

Figure 5(*b*) shows the growth rate of the perturbation versus wavenumber. With the increase of the water supply rate, the most unstable wavenumber decreases, corresponding to a longer wavelength. Figure 5(*c*) shows the dependence of the ripple wavelength on $qpl$. As shown in the figure, the computed wavelength increases gradually with the



https://doi.org/10.1017/jfm.2025.10265 Published online by Cambridge University Press

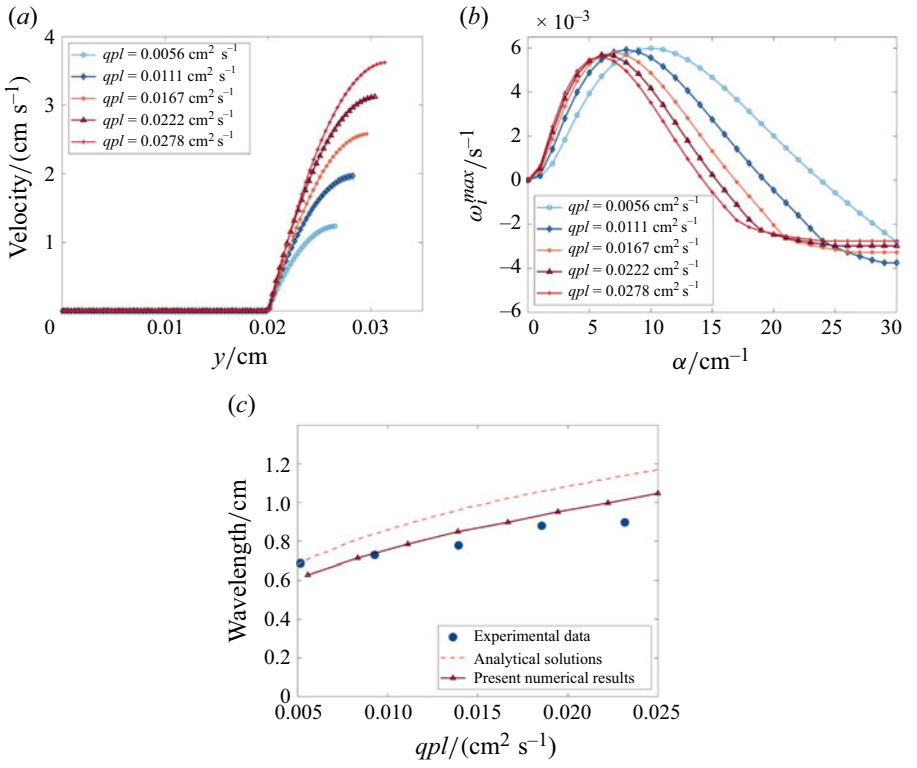



Figure 5. (*a*) Velocity profiles of base states. (*b*) Dispersion relation of growth rate $\omega_i^{max}$ with wavenumber $\alpha$ at different water supply rates per width $qpl$ on the icicle surface. (*c*) Comparison of the dominant wavelength on the icicles between our numerical results with analytical and experimental results in Ueno *et al.* (2009).

increase of $qpl$, with less error than the analytical solution when comparing against the experimental data in Ueno *et al.* (2009).

## 6. Results and discussion

### 6.1. *Results of two-phase flows*

We first study the relationship between the wavenumber $\alpha$ and the growth rate $\omega_i^{max}$ of two-phase flows. For air–water or air–ice systems, where the air layer is situated above the water or ice layer with zero base flow velocities, these set-ups represent typical stable configurations. Therefore, this section focuses on the two-phase flow with the water layer above the ice layer.

The base state of the phase field order parameter $c_0$ is shown in figure 6(*a*), where $c_0$ divides the domain into three regions: a water layer ($y = 0-30$ mm), an ice layer ($y = 30.5-60.5$ mm), and an interface region ($y = 30-30.5$ mm). Notably, the thicknesses of both the water and ice layers are significantly greater than the thickness of the interface region. In this system, with the denser water layer positioned above the lighter ice layer, and gravity acting downwards, the conditions are favourable for the onset of R–T instability.

The growth rate $\omega_i^{max}$ for different wavenumbers $\alpha$ in this two-phase flow is shown in figure 6(*b*). As $\alpha$ increases, $\omega_i^{max}$ reaches its maximum value at $\alpha_{dom} = 0.07$ mm$^{-1}$, after which it decreases, corresponding to a dominant wavelength $2\pi/(0.07\ \text{mm}^{-1}) = 90$ mm.



https://doi.org/10.1017/jfm.2025.10265 Published online by Cambridge University Press

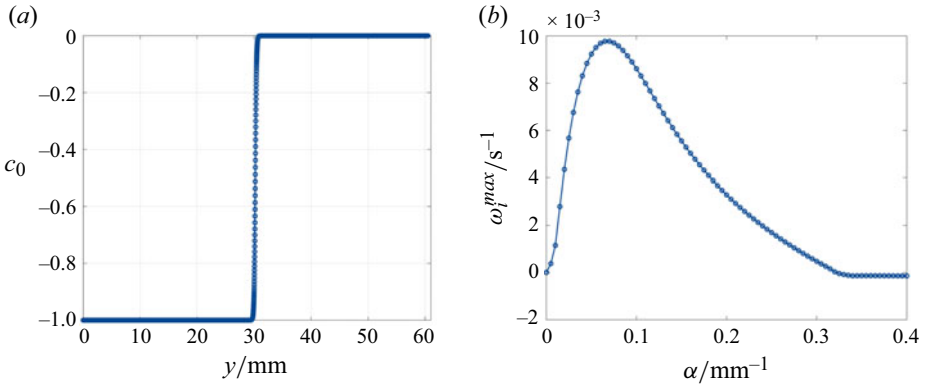



Figure 6. (*a*) Phase-field order parameter $c_0$ for the base states of the water–ice flow. (*b*) Dispersion relation of growth rate $\omega_i^{max}$ with wavenumber $\alpha$ of the water–ice flow.

This value is in agreement with the dominant wavelength predicted by the R–T instability theory for incompressible, inviscid and immiscible two-phase flow with a motionless base velocity. According to the theory, the dominant wavelength is given by $2\sqrt{3}\,\pi(\sigma_c/(\Delta\rho\, g))^{1/2} = 94$ mm, where $\Delta\rho$ is the density difference between water and ice (Drazin 2002; Faghri & Zhang 2006). The close match between our numerical results and the theoretical prediction further validates the accuracy of our model.

### 6.2. *Results of three-phase flows*

We then study the relationship between the wavenumber $\alpha$ and the growth rate $\omega_i^{max}$ of the ice patterns associated with the three-phase flows shown in figure 1. For the flows with three layers, the thicknesses of the water layer and the ice layer serve vital roles (Cheng *et al.* 2014). Figures 7(*a–c*) and 7(*d–f*) illustrate $\omega_i^{max}$ versus $\alpha$ at different ice layer thicknesses $l_{ice}$, and water layer thicknesses $l_{water}$, respectively. For a given wavenumber, the growth rate increases with either $l_{ice}$ or $l_{water}$. The yellow dashed line in figure 7(*f*) and the red bars in figure 7(*g*) depict $\alpha_{dom}$ reducing from 0.2 mm$^{-1}$ to 0.07 mm$^{-1}$ with the increase of $l_{water}$ at a thick enough ice layer ($l_{ice} = 30$ mm). It is intriguing to note that the critical wavenumber $\alpha_{cr}$, which distinguishes the stable and unstable regions, robustly takes a value approximately 0.32 mm$^{-1}$ regardless of the thickness of the water or ice layers (see white dotted lines on the right-hand sides of figure 7(*a–f*), and the grey bars in figure 7*g*). This critical value indicates that the pattern of ice ripples has a minimum possible wavelength.

The variation of $\alpha_{dom}$ with respect to $l_{ice}$ and $l_{water}$ is examined, as shown in figure 7(*h*). A larger value of either $l_{ice}$ or $l_{water}$ corresponds to smaller dominant wavenumbers, saturating at $\alpha_{dom} = 0.07$ mm$^{-1}$, indicating that thicker water and ice layers lead to longer wavelength ripples. Our results demonstrate that for a given $l_{ice}$, with the increase of $l_{water}$, $\alpha_{dom}$ decreases, indicating an approximate inverse proportionality between $\alpha_{dom}$ and $l_{water}$. Such a relationship can be expressed as $\alpha_{dom} = e_1 + 1/(e_2 l_{water} + e_3)$, and similarly, for a given $l_{water}$, $\alpha_{dom}$ and $l_{ice}$ show an approximate inverse proportionality, $\alpha_{dom} = e_4 + 1/(e_5 l_{ice} + e_6)$, where $e_1 - e_6$ are constants. To account for both proportionalities simultaneously, we introduce a comprehensive expression for $\alpha_{dom}$ that considers varying $l_{water}$ and $l_{ice}$:

$$\alpha_{dom} = \frac{C_1 l_{water} + C_2 l_{ice}}{(l_{water} + C_3)(l_{ice} + C_4)}, \tag{6.1}$$



https://doi.org/10.1017/jfm.2025.10265 Published online by Cambridge University Press

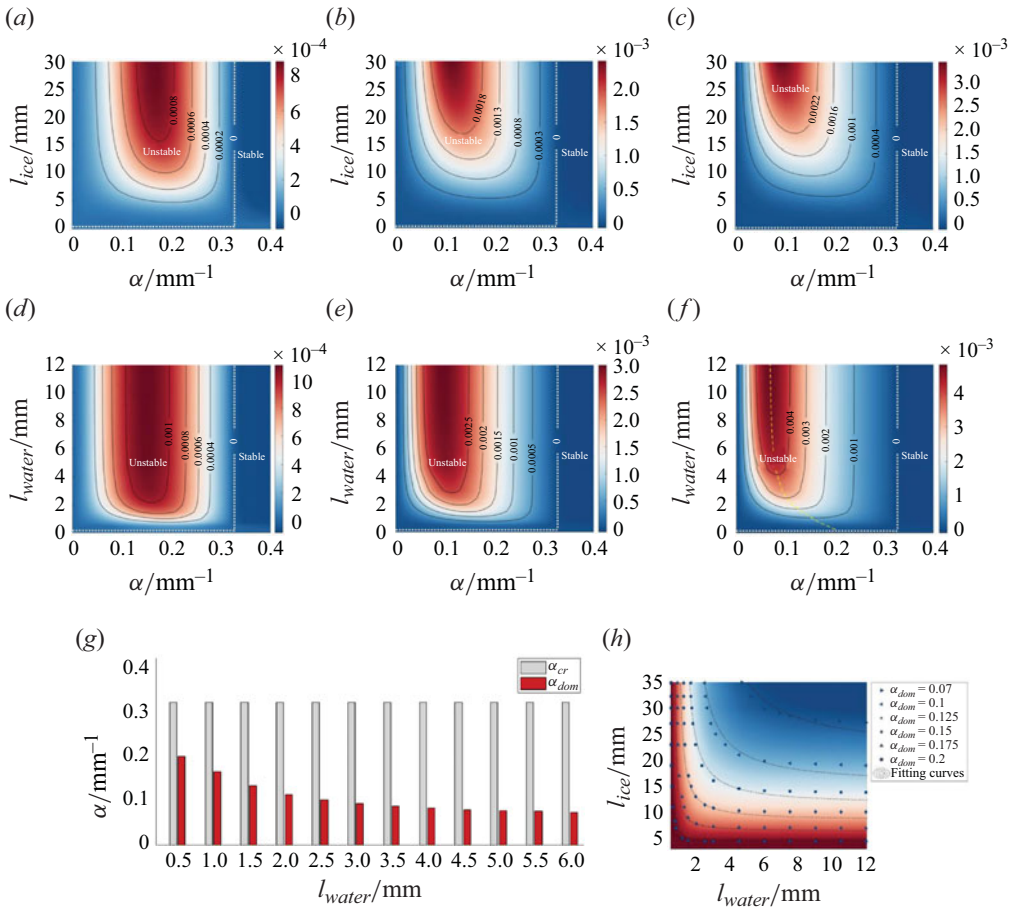



Figure 7. Dispersion relations of ice–water–air flows with different ice and water layer thicknesses. (*a–c*) Contours of growth rate $\omega_i^{max}$ (s$^{-1}$) on the $l_{ice}-\alpha$ plane with water thicknesses 1, 2 and 3 mm, respectively. (*d–f*) Contours of growth rate $\omega_i^{max}$ on the $l_{water}-\alpha$ plane with ice thicknesses 10, 20 and 30 mm, respectively. (*g*) Critical and dominant wavenumbers $\alpha_{cr}$ and $\alpha_{dom}$ versus $l_{water}$ ($l_{ice} = 30$ mm). (*h*) Contours of $\alpha_{dom}$ on the $l_{ice}-l_{water}$ plane, where the points are numerical results, and the lines are the fitting curves.

where $C_1 = 2.21$, $C_2 = 0.19$, $C_3 = 0.40$ and $C_4 = 6.33$ are obtained by fitting the numerical results using the least squares method. The results predicted by (6.1) are presented in figure 7(*h*) as lines, which agree well with the numerical ones (shown with points). In the scenario where the ice layer thickness approaches infinity and $l_{ice} \gg l_{water}$, (6.1) reduces to $\alpha_{dom} \approx C_2/(l_{water} + C_3) \leqslant 0.475$ mm$^{-1}$, which indicates a maximum dominant wavenumber for the ice patterns. Similarly, $\alpha_{dom} \approx C_1/(l_{ice} + C_4) \leqslant 0.35$ mm$^{-1}$ is the maximum dominant wavenumber for cases with an infinite water layer thickness.

As shown in figure 8(*a*), it is worth noting that the instability disappears when removing the gravity term or artificially setting the density of ice to be higher than water. Therefore, the instability is analogous to the R–T instability occurring when a denser fluid is placed above a lighter one. When the interface is slightly deformed, the denser fluid tends to sink and permeate the lighter one below, causing a decrease in the gravitational potential of the entire system (Li *et al.* 2022). Such gravity-driven instability has been



https://doi.org/10.1017/jfm.2025.10265 Published online by Cambridge University Press

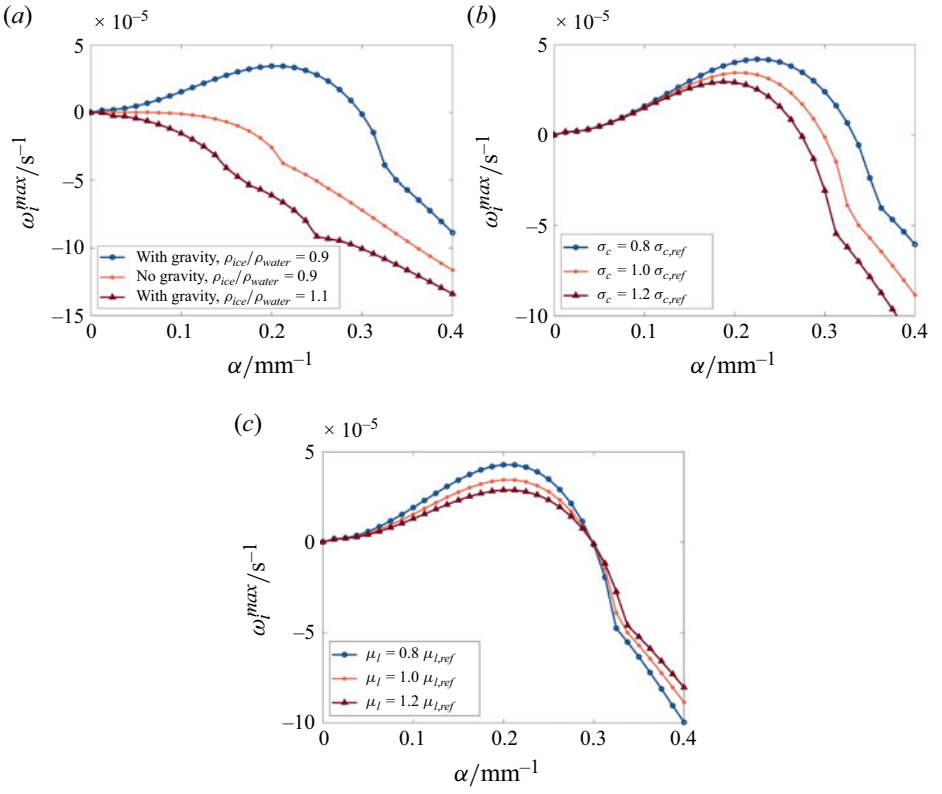



Figure 8. Dispersion relations of growth rate $\omega_i^{max}$ with wavenumber $\alpha$ for (*a*) gravity, (*b*) surface tension $\sigma_c$ ($\sigma_{c,ref} = 0.0727$ N m$^{-1}$), and (*c*) viscosity of water $\mu_l$ ($\mu_{l,ref} = 0.001$ Pa s) effects with $l_{ice} = l_{water} = 2$ mm.

conventionally studied in fluid–fluid interfaces and most recently found in elastic solid–fluid ones (Terrones 2005; Piriz, Sun & Tahir 2013). For the R–T instability of three-layer flow, it has been demonstrated analytically that the instability is relevant to the thickness of the interlayer (Parhi & Nath 1991; Cheng *et al.* 2014). The growth rate of the system increases with the interlayer thickness due to the coupling effects of the three-layer flows (Cheng *et al.* 2014), which aligns with our findings. When the interlayer is thick enough, the coupling effect fades away, and the instability of each interface will develop separately (Cheng *et al.* 2014). Therefore, when the water layer is thick enough, the instability of the system is mainly influenced by the ice–water interface since the water–air interface is stable, and the instability of the three-layer system is equivalent to that of the ice–water flow. When $l_{ice}$ or $l_{water}$ tends to zero, the system reduces to a two-phase flow (either water–air or ice–air) with zero base velocity and a denser lower layer, which is stable, as marked by the horizontal white dotted lines in figure 7(*a–f*), matching physical observations and the mechanism of the R–T instability.

The dispersion relations of growth rate $\omega_i^{max}$ with wavenumber $\alpha$ at different surface tensions at the ice–water interface, $\sigma_c$, are shown in figure 8(*b*). The results illustrate that as $\sigma_c$ increases, the growth rate decreases, demonstrating that surface tension acts to suppress instability. We note that this result is reasonable, as surface tension generally tends to smooth the interface and inhibit the development of wave perturbations. Moreover, the most unstable wavenumber $\alpha_{dom}$ decreases with the increase of $\sigma_c$, indicating a larger

https://doi.org/10.1017/jfm.2025.10265 Published online by Cambridge University Press

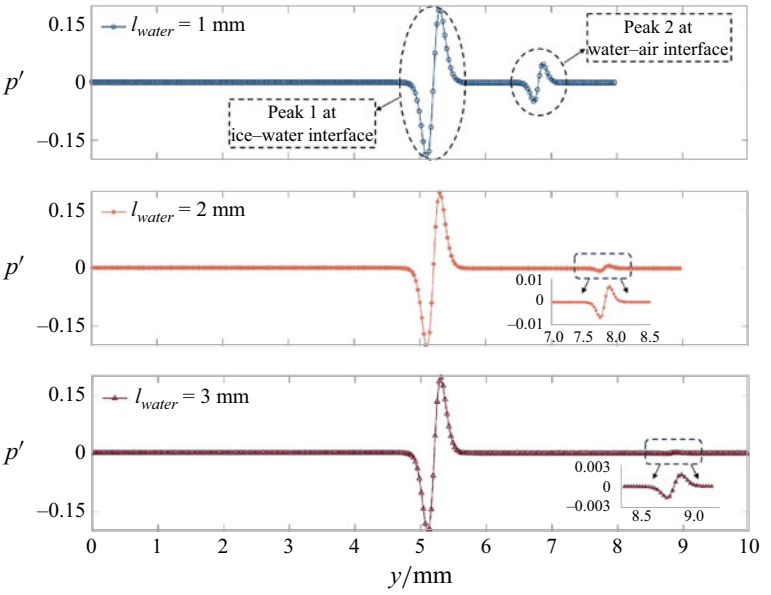



Figure 9. Distributions of the most unstable mode along the $y$ direction at different values of $l_{water}$ ($l_{ice} = 5$ mm, $\alpha = 0.3$ mm$^{-1}$), illustrated by the pressure perturbation. The two peaks – a stronger one at the water–ice interface, and a weaker one at the water–air interface – are denoted as Peak 1 and Peak 2, respectively.

wavelength for bigger $\sigma_c$, which is also consistent with the typical R–T instability theory (Drazin 2002; Faghri & Zhang 2006). The dispersion relations at different viscosities of water, $\mu_l$, are shown in figure 8($c$). Similar to surface tension $\sigma_c$, an increase in $\mu_l$ leads to a decrease in the growth rate, indicating that viscosity also acts as a damping term. However, unlike surface tension, viscosity does not affect the most unstable wavenumber.

We then compare the computational results with the natural observations. The upper right corner of figure 7($h$) shows that when the ice and water layers are thick enough, the dominant wavelength converges to 0.07 mm$^{-1}$, corresponding to wavelength 90 mm, in good agreement with the observations in figure 1($a$), where the wavelength of the glacier is approximately 0.1 m (Camporeale & Ridolfi 2012*b*). This value is also close to the dominant wavelength 94 mm predicted by the R–T instability theory (see § 6.1). Further, a positive correlation between water layer thickness and wavelength of ripples illustrated in figure 7($d$–$f$) is supported by the observed ice ripples on the lake depicted in figure 1($b$). It is noteworthy that positions with thicker water coverage on both sides of figure 1($b$) exhibit longer wavelength ripples, whereas positions with thinner water in the middle exhibit shorter wavelengths.

### 6.3. *Profiles of the most unstable mode*

Though it has been reported that the unstable perturbations are mainly displaced on the interfaces of two-phase flows (Camporeale & Ridolfi 2012*b*; Boomkamp *et al.* 1997), not much effort has been devoted to investigating three-phase flows, or the profile of the disturbance. Here, the distribution of the most unstable mode in the present three-phase flow is shown in figure 9, where we note that it illustrates two peaks. The first peak (Peak 1) is concentrated around the ice–water interface, while the second one (Peak 2) is associated with the water–air interface. The perturbation is manifested physically in terms of pressure $p'$, or can be illustrated geometrically in terms of $\phi'$ and $c'$ (not shown here for brevity). The formation of the disturbance at Peak 2 is recognised as the propagation of waves at



https://doi.org/10.1017/jfm.2025.10265 Published online by Cambridge University Press

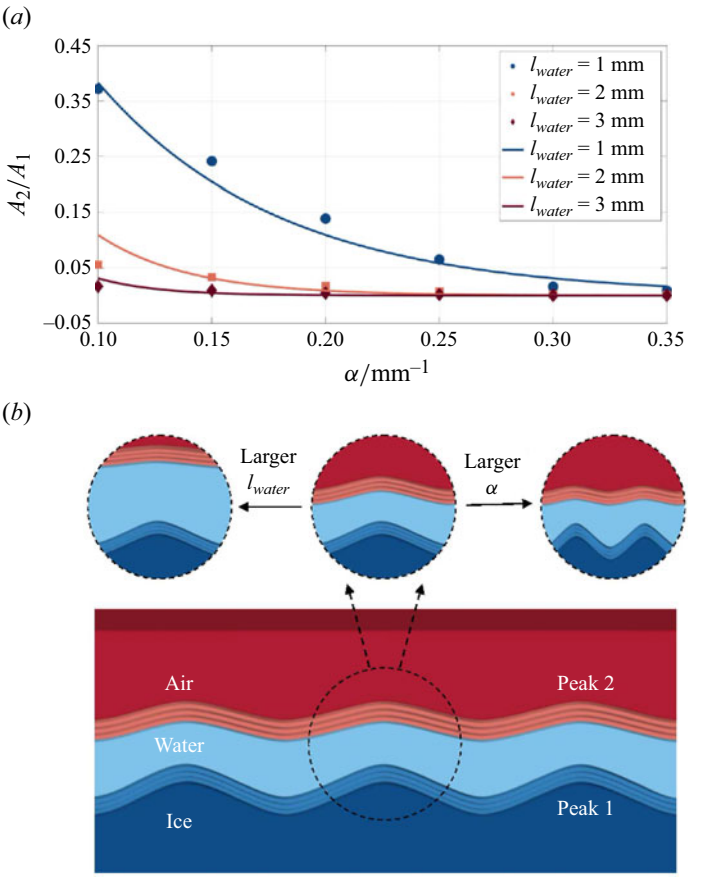



Figure 10. (*a*) The amplitude ratio of Peak 2 to Peak 1, where the points are numerical results, and the lines are the fitting curves. (*b*) Schematic diagram of the instability over the three phases at different $l_{water}$ and $\alpha$.

Peak 1 from the ice–water interface to the water–air interface. An increase in the thickness of the water layer results in a reduction of the effect of the perturbation at the ice–water interface to that at the water–air interface through a 'buffer layer', i.e. the water. This attenuation of perturbation transmission leads to a weakening of Peak 2, as observed in figure 9. It is worth emphasising that Peak 2 emerges only when Peak 1 is present. In cases where there is no Peak 1 at the ice–water interface, signifying the absence of ice or water, i.e. ice–air or water–air flows, Peak 2 vanishes as well, indicating that unstable perturbations will no longer exist. This conclusion aligns with the findings in figure 7(*a–f*) (see the horizontal white dotted lines).

Finally, it is of interest to establish a theoretical framework for the relations between the two peaks. The amplitude ratio of Peak 2 to Peak 1 ($A_2/A_1$) at different $l_{water}$ and $\alpha$ is depicted in figure 10(*a*). Similar to the increase of $l_{water}$, an increase in wavenumber can also lead to the weakening of Peak 2, indicating that perturbations with shorter wavelengths are less able to reach the water–air interface. This is because the viscous diffusion effect within the buffer layer increases with the wavenumber. Such decay with respect to the propagation distance was reported to be exponential in sound wave attenuation (Straka *et al.* 2013). As $l_{water}$ has a similar effect to $\alpha$ on the decay, we can expect the function to be fitted as $A_2/A_1 = B_1 \exp(-B_2 \alpha l_{water})$, where $B_1 = 1.34$ and $B_2 = 12.5$ are constants



https://doi.org/10.1017/jfm.2025.10265 Published online by Cambridge University Press

obtained by fitting the numerical results. The comparison between the fitted curves and the numerical results is shown in figure 10(*a*). The exponential relation also demonstrates that Peak 2 will vanish when the water layer is thick enough, as the perturbations at Peak 1 will be completely absorbed by the thick water. A more intuitive schematic diagram of the perturbation distribution through a thin water layer and the two peaks is shown in figure 10(*b*), where the thin water layer is deformed by the disturbance at the ice–water interface. This deformation is then transmitted to the water–air interface, demonstrating that the patterns on the ice surfaces shown in figure 1 are concentrated mainly at the ice–water interface as well as the water–air interface for cases with thinner water layer, while the patterns grow only at the ice–water interface when the water layer is thick enough.

## 7. Conclusions

In summary, we establish a theoretical framework based on the phase-field method to study the morphological patterns on ice surfaces covered by air-surrounded water flows, which takes essential steps towards unravelling the mysteries of natural pattern formation on ice surfaces. The established model is validated by predicting the wavelength of icicle ripples and comparing it against experimental data. Afterwards, the model is utilised to study the ripples on horizontal ice surfaces, e.g. glaciers and icy lakes.

We demonstrate that the emergence of ice ripples is triggered by an instability originating from the phase interfaces. The relationship between the wavenumber and growth rate of infinitesimal perturbations at various ice and water layer thicknesses is then obtained, illustrating that larger $l_{ice}$ and $l_{water}$ correspond to patterns with larger wavelengths. When $l_{ice}$ or $l_{water}$ tends to 0, corresponding to the reduction of the three-phase flow to ice–air or water–air flow, the instability vanishes. The computational results predict dominant wavelength 90 mm, aligning with the observations of the patterns on the ice surface. This wavelength can be used to model the surface roughness and also shed light on the resolution requirement in numerical simulations of icing over complex geometries.

Considering that gravity is critical to trigger the instability, and ice is lighter than liquid water, the present instability is analogous to the R–T instability. In contrast to gravity, our results show that surface tension and viscosity serve to suppress the instability. The predicted dominant wavelength 90 mm is also consistent with the typical R–T instability theory. It is worth noting that our model can be applied not only in analysing the gravity-driven R–T type instability, but also in studying other kinds of instabilities, such as icicle ripples driven by surface flows. Furthermore, the ability to handle three-phase flows with phase changes, and to analyse the effects of water and ice thicknesses on the dominant wavelength, highlights the advantages of our model over the typical R–T theory.

Moreover, based on our three-phase model, the profiles of the perturbations are presented, primarily illustrating two peaks concentrated at the ice–water and water–air interfaces. Furthermore, a theoretical framework is established to explain the exponential-form correlation between the amplitudes of the two peaks with respect to $l_{water}$ and wavenumber $\alpha$.

Overall, this linear stability research contributes to the fundamental understanding of the mechanism of pattern formation on the ice surface, and paves the way for further studies on the impact of wind speed, temperature, pressure, other surface conditions and nonlinear interactions on the icing process.

**Funding.** This work was supported by the China Scholarship Council, the National Natural Science Foundation of China (grant nos 92152109, 11988102), the ARCHER2-eCSE05-6 project, and the EU H2020-MSCA-RISE-2017 project CTFF (Control of Turbulent Friction Force, grant no. 777717).



https://doi.org/10.1017/jfm.2025.10265 Published online by Cambridge University Press

**Declaration of interests.** The authors report no conflict of interest.

**Data availability statement.** The data that support the findings of this study are available from the corresponding author upon request.

**Author contributions.** Z.W. derived the theory, performed the simulations and formal analysis, wrote the original draft, and created visualisations. K.-S.C. and S.L. contributed to the formal analysis, review and supervision. C.S. contributed to the formal analysis, review and validation. X.M. conceptualised the study, developed the methodology, performed formal analysis and investigation, and contributed to writing, review and supervision.

## Appendix A. The stability equation

The non-zero elements in the stability equation (2.10) are given below with $\theta$ the inclined angle between the flow direction $x$ and the horizontal plane. Here, $\theta = 0$ is applied for the flows on the horizontal glacier and lake shown in figure 1, while for icicles in § 5, $\theta = \pi/2$ is applied since the flows are vertical to the horizontal line. The velocity vector $\boldsymbol{u}'$ is expanded into $u'_x$ and $u'_y$, and $u_0$ and $v_0$ are used to denote the corresponding base flow velocities, respectively. We note that the base flow is steady ($\partial \boldsymbol{q}_0/\partial t = 0$) and independent of $x$ ($\partial \boldsymbol{q}_0/\partial x = 0$), and the base velocity is parallel to the $x$ direction ($v_0 = 0$).

$$
\begin{gathered}
\boldsymbol{\Gamma}(1,1) = \boldsymbol{\Gamma}(2,2) = -\rho_0, \\
\boldsymbol{\Gamma}(3,4) = \tfrac{1}{2}(\phi_0 + 1)(\rho_l - \rho_s), \\
\boldsymbol{\Gamma}(3,5) = \tfrac{1}{2}[(c_0 + 1)\rho_l - c_0\rho_s - \rho_g)], \\
\boldsymbol{\Gamma}(4,4) = \boldsymbol{\Gamma}(5,5) = 1, \\
\boldsymbol{\Gamma}(7,4) = -\frac{1}{2}(\phi_0 + 1)L - \frac{1}{2}c_{p0}T_0[(\phi_0 + 1)(\rho_l - \rho_s)] \\
-\frac{1}{2}\rho_0 T_0[(\phi_0 + 1)(c_{pl} - c_{ps})], \\
\boldsymbol{\Gamma}(7,5) = -\frac{1}{2}c_0 L - \frac{1}{2}c_{p0}T_0[(c_0 + 1)\rho_l - c_0\rho_s - \rho_g] \\
-\frac{1}{2}\rho_0 T_0[(c_0 + 1)c_{pl} - c_0 c_{ps} - c_{pg}], \\
\boldsymbol{\Gamma}(7,7) = -\rho_0 c_{p0},
\end{gathered}
\tag{A1}
$$

$$
\begin{gathered}
\boldsymbol{H}_x(1,1) = -\rho_0 u_0, \\
\boldsymbol{H}_x(1,2) = \frac{1}{Re}\frac{\partial \mu_0}{\partial y}, \\
\boldsymbol{H}_x(1,3) = -1, \\
\boldsymbol{H}_x(1,4) = -\frac{3}{2\sqrt{2}}\frac{Cn_1}{We_1}\frac{\partial^2 c_0}{\partial y^2}, \\
\boldsymbol{H}_x(1,5) = -\frac{3}{2\sqrt{2}}\frac{Cn_2}{We_2}\frac{\partial^2 \phi_0}{\partial y^2}, \\
\boldsymbol{H}_x(2,1) = -\frac{2}{3}\frac{1}{Re}\frac{\partial \mu_0}{\partial y},
\end{gathered}
$$



https://doi.org/10.1017/jfm.2025.10265 Published online by Cambridge University Press

$$\boldsymbol{H}_x(2,2) = -\rho_0 u_0,$$
$$\boldsymbol{H}_x(2,4) = \frac{1}{2}\frac{1}{Re}\frac{\partial u_0}{\partial y}(\phi_0+1)(\mu_l-\mu_s),$$
$$\boldsymbol{H}_x(2,5) = \frac{1}{2}\frac{1}{Re}\frac{\partial u_0}{\partial y}[(c_0+1)\mu_l - c_0\mu_s - \mu_g],$$
$$\boldsymbol{H}_x(3,1) = \rho_0,$$
$$\boldsymbol{H}_x(3,4) = \tfrac{1}{2}u_0(\phi_0+1)(\rho_l-\rho_s),$$
$$\boldsymbol{H}_x(3,5) = \tfrac{1}{2}u_0[(c_0+1)\rho_l - c_0\rho_s - \rho_g],$$
$$\boldsymbol{H}_x(4,1) = c_0,$$
$$\boldsymbol{H}_x(4,4) = \boldsymbol{H}_x(5,5) = u_0,$$
$$\boldsymbol{H}_x(7,1) = -\rho_0 c_{p0} T_0,$$
$$\boldsymbol{H}_x(7,2) = 2\frac{Ec}{Re}\mu_0\frac{\partial u_0}{\partial y},$$
$$\boldsymbol{H}_x(7,4) = -\frac{1}{2}c_{p0}T_0u_0(\phi_0+1)(\rho_l-\rho_s)$$
$$-\frac{1}{2}\rho_0 T_0 u_0(\phi_0+1)(c_{pl}-c_{ps}),$$
$$\boldsymbol{H}_x(7,5) = -\frac{1}{2}c_{p0}T_0u_0[(c_0+1)\rho_l - c_0\rho_s - \rho_g]$$
$$-\frac{1}{2}\rho_0 T_0 u_0[(c_0+1)c_{pl} - c_0 c_{ps} - c_{pg}],$$
$$\boldsymbol{H}_x(7,7) = -\rho_0 c_{p0} u_0, \tag{A2}$$

$$\boldsymbol{H}_y(1,1) = \frac{1}{Re}\frac{\partial \mu_0}{\partial y},$$
$$\boldsymbol{H}_y(1,4) = \frac{1}{2}\frac{1}{Re}\frac{\partial u_0}{\partial y}(\phi_0+1)(\mu_l-\mu_s),$$
$$\boldsymbol{H}_y(1,5) = \frac{1}{2}\frac{1}{Re}\frac{\partial u_0}{\partial y}[(c_0+1)\mu_l - c_0\mu_s - \mu_g],$$
$$\boldsymbol{H}_y(2,2) = \frac{4}{3}\frac{1}{Re}\frac{\partial \mu_0}{\partial y},$$
$$\boldsymbol{H}_y(2,3) = -1,$$
$$\boldsymbol{H}_y(2,4) = -\frac{3}{2\sqrt{2}}\frac{Cn_1}{We_1}\frac{\partial^2 c_0}{\partial y^2},$$
$$\boldsymbol{H}_y(2,5) = -\frac{3}{2\sqrt{2}}\frac{Cn_2}{We_2}\frac{\partial^2 \phi_0}{\partial y^2},$$
$$\boldsymbol{H}_y(3,2) = \rho_0,$$



https://doi.org/10.1017/jfm.2025.10265 Published online by Cambridge University Press

$$\boldsymbol{H}_y(4,2) = c_0,$$

$$\boldsymbol{H}_y(7,1) = 2\frac{Ec}{Re}\mu_0\frac{\partial u_0}{\partial y},$$

$$\boldsymbol{H}_y(7,2) = -\rho_0 c_{p0} T_0,$$

$$\boldsymbol{H}_y(7,4) = \frac{1}{2}\frac{1}{Re\,Pr}\frac{\partial T_0}{\partial y}(\phi_0+1)(\kappa_l-\kappa_s),$$

$$\boldsymbol{H}_y(7,5) = \frac{1}{2}\frac{1}{Re\,Pr}\frac{\partial T_0}{\partial y}[(c_0+1)\kappa_l - c_0\kappa_s - \kappa_g],$$

$$\boldsymbol{H}_y(7,7) = \frac{1}{Re\,Pr}\frac{\partial \kappa_0}{\partial y}, \tag{A3}$$

$$\boldsymbol{H}(1,2) = -\rho_0\frac{\partial u_0}{\partial y},$$

$$\boldsymbol{H}(1,4) = \frac{1}{2}\frac{1}{Re}\frac{\partial u_0}{\partial y}\frac{\partial \phi_0}{\partial y}(\mu_l-\mu_s) + \frac{1}{2}\frac{1}{Re}\frac{\partial^2 u_0}{\partial y^2}(\phi_0+1)(\mu_l-\mu_s)$$
$$+\frac{1}{2}\frac{\sin\theta}{Fr^2}(\phi_0+1)(\rho_l-\rho_s),$$

$$\boldsymbol{H}(1,5) = \frac{1}{2}\frac{1}{Re}\frac{\partial u_0}{\partial y}\frac{\partial c_0}{\partial y}(\mu_l-\mu_s) + \frac{1}{2}\frac{1}{Re}\frac{\partial^2 u_0}{\partial y^2}[(c_0+1)\mu_l - c_0\mu_s - \mu_g]$$
$$+\frac{1}{2}\frac{\sin\theta}{Fr^2}[(c_0+1)\rho_l - c_0\rho_s - \rho_g],$$

$$\boldsymbol{H}(2,4) = -\frac{1}{2}\frac{\cos\theta}{Fr^2}(\phi_0+1)(\rho_l-\rho_s),$$

$$\boldsymbol{H}(2,5) = -\frac{1}{2}\frac{\cos\theta}{Fr^2}[(c_0+1)\rho_l - c_0\rho_s - \rho_g],$$

$$\boldsymbol{H}(3,2) = \frac{\partial \rho_0}{\partial y},$$

$$\boldsymbol{H}(4,2) = \frac{\partial c_0}{\partial y},$$

$$\boldsymbol{H}(4,4) = \frac{M_{nc}}{Cn_1}(6c_0^2+6c_0+1) - 2M_{nl}(T_0-1)c_0(c_0+1)(2c_0+1),$$

$$\boldsymbol{H}(4,7) = -M_{nl}c_0^2(c_0+1)^2,$$

$$\boldsymbol{H}(5,2) = \frac{\partial \phi_0}{\partial y},$$

$$\boldsymbol{H}(6,5) = \frac{1-3\phi_0^2}{Cn_2},$$

$$\boldsymbol{H}(6,6) = 1,$$

$$\boldsymbol{H}(7,1) = \frac{Ec}{Fr^2}\rho_0\sin\theta,$$



https://doi.org/10.1017/jfm.2025.10265 Published online by Cambridge University Press

$$\boldsymbol{H}(7,2) = -\frac{\partial(\rho_0 c_{p0} T_0)}{\partial y} - \frac{Ec}{Fr^2}\rho_0 \cos\theta,$$

$$\boldsymbol{H}(7,4) = \frac{1}{2}\frac{1}{Re\ Pr}\frac{\partial T_0}{\partial y}\frac{\partial \phi_0}{\partial y}(\kappa_l - \kappa_s) + \frac{1}{2}\frac{1}{Re\ Pr}\frac{\partial^2 T_0}{\partial y^2}(\phi_0 + 1)(\kappa_l - \kappa_s)$$
$$+\frac{1}{2}\frac{Ec}{Re}\left(\frac{\partial u_0}{\partial y}\right)^2(\phi_0 + 1)(\mu_l - \mu_s)$$
$$+\frac{1}{2}\frac{Ec}{Fr^2}u_0 \sin\theta(\phi_0 + 1)(\rho_l - \rho_s),$$

$$\boldsymbol{H}(7,5) = \frac{1}{2}\frac{1}{Re\ Pr}\frac{\partial T_0}{\partial y}\frac{\partial c_0}{\partial y}(\kappa_l - \kappa_s) + \frac{1}{2}\frac{1}{Re\ Pr}\frac{\partial^2 T_0}{\partial y^2}[(c_0 + 1)\kappa_l - c_0\kappa_s - \kappa_g]$$
$$+\frac{1}{2}\frac{Ec}{Re}\left(\frac{\partial u_0}{\partial y}\right)^2[(c_0 + 1)\mu_l - c_0\mu_s - \mu_g]$$
$$+\frac{1}{2}\frac{Ec}{Fr^2}u_0 \sin\theta[(c_0 + 1)\rho_l - c_0\rho_s - \rho_g], \tag{A4}$$

$$\boldsymbol{H}_{xx}(1,1) = \frac{4}{3}\frac{\mu_0}{Re},$$
$$\boldsymbol{H}_{xx}(2,2) = \frac{\mu_0}{Re},$$
$$\boldsymbol{H}_{xx}(2,4) = -\frac{3}{2\sqrt{2}}\frac{Cn_1}{We_1}\frac{\partial c_0}{\partial y},$$
$$\boldsymbol{H}_{xx}(2,5) = -\frac{3}{2\sqrt{2}}\frac{Cn_2}{We_2}\frac{\partial \phi_0}{\partial y},$$
$$\boldsymbol{H}_{xx}(4,4) = -M_{nc}Cn_1,$$
$$\boldsymbol{H}_{xx}(5,6) = -M_{n\phi},$$
$$\boldsymbol{H}_{xx}(6,5) = Cn_2,$$
$$\boldsymbol{H}_{xx}(7,7) = \frac{\kappa_0}{Re\ Pr}, \tag{A5}$$
$$\boldsymbol{H}_{yy}(1,1) = \frac{\mu_0}{Re},$$
$$\boldsymbol{H}_{yy}(2,2) = \frac{4}{3}\frac{\mu_0}{Re},$$
$$\boldsymbol{H}_{yy}(2,4) = -\frac{3}{2\sqrt{2}}\frac{Cn_1}{We_1}\frac{\partial c_0}{\partial y},$$
$$\boldsymbol{H}_{yy}(2,5) = -\frac{3}{2\sqrt{2}}\frac{Cn_2}{We_2}\frac{\partial \phi_0}{\partial y},$$
$$\boldsymbol{H}_{yy}(4,4) = -M_{nc}Cn_1,$$
$$\boldsymbol{H}_{yy}(5,6) = -M_{n\phi},$$
$$\boldsymbol{H}_{yy}(6,5) = Cn_2,$$
$$\boldsymbol{H}_{yy}(7,7) = \frac{\kappa_0}{Re\ Pr}, \tag{A6}$$



https://doi.org/10.1017/jfm.2025.10265 Published online by Cambridge University Press

$$\boldsymbol{H}_{xy}(1,2) = \boldsymbol{H}_{xy}(2,1) = \frac{1}{3}\frac{\mu_0}{Re}. \tag{A7}$$

Here, $Re$ denotes the Reynolds number, $Fr$ is the Froude number, $Pr$ is the Prandtl number, $Ec$ is the Eckert number, $We_1$ and $We_2$ are Weber numbers, $Cn_1$ and $Cn_2$ represent the Cahn numbers, and $M_{nc}$, $M_{n\phi}$ and $M_{nl}$ denote the mobility numbers. These numbers are defined as

$$\begin{aligned}
&Re = \frac{\rho_r u_r d_r}{\mu_r}, \quad Fr = \frac{u_r}{\sqrt{g d_r}}, \quad Pr = \frac{\mu_r c_{pr}}{\kappa_r}, \quad Ec = \frac{u_r^2}{c_{pr} T_r},\\
&We_1 = \frac{u_r^2 \rho_r d_r}{\sigma_c}, \quad We_2 = \frac{u_r^2 \rho_r d_r}{\sigma_\phi}, \quad Cn_1 = \frac{\xi_c}{d_r}, \quad Cn_2 = \frac{\xi_\phi}{d_r},\\
&M_{nc} = \frac{6 M_c \sigma_c}{u_r}, \quad M_{n\phi} = \frac{3 M_\phi \sigma_\phi}{2\sqrt{2} u_r d_r^2}, \quad M_{nl} = \frac{30 M_c L d_r}{u_r},
\end{aligned} \tag{A8}$$

where the subscript $r$ denotes the reference values, $d_r$, $u_r$ and $T_r = T_M$ represent the reference thickness, the reference velocity and the reference temperature, respectively, and $\boldsymbol{u}$, $t$, $p$, $\rho$, $T$, $\mu$, $\kappa$, $c_p$, $\nabla$ and $L$ are non-dimensionalised by $u_r$, $d_r/u_r$, $\rho_r u_r^2$, $\rho_r$, $T_r$, $\mu_r$, $\kappa_r$, $c_{pr}$, $d_r$ and $\rho_r c_{pr} T_r$, respectively.

## References


Adkins, R., Shelton, E.M., Renoult, M.-C., Carles, P. & Rosenblatt, C. 2017 Interface coupling and growth rate measurements in multilayer Rayleigh–Taylor instabilities. *Phys. Rev. Fluids* **2** (6), 062001.

Allen, S.M. & Cahn, J.W. 1979 A microscopic theory for antiphase boundary motion and its application to antiphase domain coarsening. *Acta. Metall.* **27** (6), 1085–1095.

Aslangil, D. & Wong, M.L. 2023 Investigation of strong isothermal stratification effects on multi-mode compressible Rayleigh–Taylor instability. *Phys. Fluids* **35** (8), 084116.

Badillo, A. 2012 Quantitative phase-field modeling for boiling phenomena. *Phys. Rev. E* **86** (4), 041603.

Blackburn, J. & She, Y. 2019 A comprehensive public-domain river ice process model and its application to a complex natural river. *Cold Reg. Sci. Technol.* **163**, 44–58.

Boettinger, W.J., Warren, J.A., Beckermann, C. & Karma, A. 2002 Phase-field simulation of solidification. *Annu. Rev. Mater. Sci.* **32** (1), 163–194.

Boomkamp, P.A.M., Boersma, B.J., Miesen, R.H.M. & Beijnon, G.V. 1997 A Chebyshev collocation method for solving two-phase flow stability problems. *J. Comput. Phys.* **132** (2), 191–200.

Bushuk, M., Holland, D.M., Stanton, T.P., Stern, A. & Gray, C. 2019 Ice scallops: a laboratory investigation of the ice–water interface. *J. Fluid Mech.* **873**, 942–976.

Cahn, J.W. & Hilliard, J.E. 1958 Free energy of a nonuniform system. I. Interfacial free energy. *J. Chem. Phys.* **28** (2), 258–267.

Camporeale, C. & Ridolfi, L. 2012*a* Hydrodynamic-driven stability analysis of morphological patterns on stalactites and implications for cave paleoflow reconstructions. *Phys. Rev. Lett.* **108** (23), 238501.

Camporeale, C. & Ridolfi, L. 2012*b* Ice ripple formation at large Reynolds numbers. *J. Fluid Mech.* **694**, 225–251.

Charru, F., Andreotti, B. & Claudin, P. 2013 Sand ripples and dunes. *Annu. Rev. Fluid Mech.* **45** (1), 469–493.

Cheng, T., Liu, S.-G., Liu, X.-Y., Hao, N., Teng, A.-P. & Li, Y.-J. 2014 Effects of density and thickness of interlayer on RT instability of interfaces. *Commun. Theor. Phys.* **61** (5), 649–653.

Dadvand, A., Bagheri, M., Samkhaniani, N., Marschall, H. & Wörner, M. 2021 Advected phase-field method for bounded solution of the Cahn–Hilliard Navier–Stokes equations. *Phys. Fluids* **33** (5), 053311.

Drazin, P.G. 2002 *Introduction to Hydrodynamic Stability*. Cambridge University Press.

Faghri, A. & Zhang, Y. 2006 *Transport Phenomena in Multiphase Systems*. Elsevier.

Gelfgat, A.Y., Bar-Yoseph, P.Z., Solan, A. & Kowalewski, T.A. 1999 An axisymmetry-breaking instability of axially symmetric natural convection. *Intl J. Transport Phenom.* **1**, 173–190.




https://doi.org/10.1017/jfm.2025.10265 Published online by Cambridge University Press

GRIVET, R., MONIER, A., HUERRE, A., JOSSERAND, C. & SÉON, T. 2022 Contact line catch up by growing ice crystals. *Phys. Rev. Lett.* **128** (25), 254501.
GUO, H.-Y., WANG, L.-F., YE, W.-H., WU, J.-F. & ZHANG, W.-Y. 2017 Rayleigh–Taylor instability of multi-fluid layers in cylindrical geometry. *Chinese Phys. B* **26** (12), 125202.
HILLIG, W.B. 1998 Measurement of interfacial free energy for ice/water system. *J. Cryst. Growth* **183** (3), 463–468.
JACOBS, J.W. & DALZIEL, S.B. 2005 Rayleigh–Taylor instability in complex stratifications. *J. Fluid Mech.* **542**, 251–279.
KASER, G., COGLEY, J.G., DYURGEROV, M.B., MEIER, M.F. & OHMURA, A. 2006 Mass balance of glaciers and ice caps: consensus estimates for 1961–2004. *Geophys. Res. Lett.* **33** (19), L19501.
KIM, J. 2012 Phase-field models for multi-component fluid flows. *Commun. Comput. Phys.* **12** (3), 613–661.
LEPPÄRANTA, M. 2010 Modelling the formation and decay of lake ice. *The Impact of Climate Change on European Lakes*. 63–83.
LI, K., ZHUO, G., ZHANG, Y., LIU, C., CHEN, W. & LÜ, C. 2022 Hypergravitational Rayleigh–Taylor instability in solids. *Extreme Mech. Lett.* **55**, 101809.
LIU, C. & SHEN, J. 2003 A phase field model for the mixture of two incompressible fluids and its approximation by a Fourier-spectral method. *Physica D* **179** (3–4), 211–228.
LUNDBEK HANSEN, J., VAN HECKE, M., HAANING, A., ELLEGAARD, C., HASTE ANDERSEN, K., BOHR, T. & SAMS, T. 2001 Instabilities in sand ripples. *Nature* **410** (6826), 324–324.
MAKKONEN, L. 1988 A model of icicle growth. *J. Glaciol.* **34** (116), 64–70.
MATSUOKA, C. 2020 Nonlinear dynamics of double-layer unstable interfaces with non-uniform velocity shear. *Phys. Fluids* **32** (10), 102109.
MCDONALD, G.D., MÉNDEZ HARPER, J., OJHA, L., CORLIES, P., DUFEK, J., EWING, R.C. & KERBER, L. 2022 Aeolian sediment transport on Io from lava–frost interactions. *Nat. Commun.* **13** (1), 2076.
MIKAELIAN, K.O. 1982 Rayleigh–Taylor instabilities in stratified fluids. *Phys. Rev. A* **26** (4), 2140–2158.
MIRJALILI, S., IVEY, C.B. & MANI, A. 2019 Comparison between the diffuse interface and volume of fluid methods for simulating two-phase flows. *Intl J. Multiphase Flow* **116**, 221–238.
MURATA, K.-I., NAGASHIMA, K. & SAZAKI, G. 2019 How do ice crystals grow inside quasiliquid layers? *Phys. Rev. Lett.* **122** (2), 026102.
OGAWA, N. & FURUKAWA, Y. 2002 Surface instability of icicles. *Phys. Rev. E* **66** (4), 041202.
PARHI, S. & NATH, G. 1991 A sufficient criterion for Rayleigh–Taylor instability of incompressible viscous three-layer flow. *Intl J. Engng Sci.* **29** (11), 1439–1450.
PIRIZ, A.R., SUN, Y.B. & TAHIR, N.A. 2013 Rayleigh–Taylor stability boundary at solid–liquid interfaces. *Phys. Rev. E* **88** (2), 023026.
POPOVIĆ, P., CAEL, B B., SILBER, M. & ABBOT, D.S. 2018 Simple rules govern the patterns of Arctic sea ice melt ponds. *Phys. Rev. Lett.* **120** (14), 148701.
Rayleigh, L. 1882 Investigation of the character of the equilibrium of an incompressible heavy fluid of variable density. *Proc. Lond. Math. Soc.* **1** (1), 170–177.
REITZLE, M., RUBERTO, S., STIERLE, R., GROSS, J., JANZEN, T. & WEIGAND, B. 2019 Direct numerical simulation of sublimating ice particles. *Intl J. Therm. Sci.* **145**, 105953.
RIGNOT, E. & KANAGARATNAM, P. 2006 Changes in the velocity structure of the Greenland ice sheet. *Science* **311** (5763), 986–990.
SABOURI-GHOMI, M., PROVATAS, N. & GRANT, M. 2001 Solidification of a supercooled liquid in a narrow channel. *Phys. Rev. Lett.* **86** (22), 5084–5087.
SATO, K. & KOSHIMURA, S. 2023 A filtering approach for the conservative Allen–Cahn equation solved by the lattice Boltzmann method and a numerical study of the interface thickness. *Intl J. Multiphase Flow* **167**, 104554.
SENGUPTA, A., ULLOA, H.N. & JOSHI, B. 2023 Multi-layer Rayleigh–Taylor instability: consequences for naturally occurring stratified mixing layers. *Phys. Fluids* **35** (10), 102110.
SHEN, J. 2011 Modeling and numerical approximation of two-phase incompressible flows by a phase-field approach. In *Multiscale Modeling and Analysis for Materials Simulation* (ed. W. Bao & Q. Du), pp. 147–195. World Scientific.
SHEN, J. & YANG, X. 2009 An efficient moving mesh spectral method for the phase-field model of two-phase flows. *J. Comput. Phys.* **228** (8), 2978–2992.
STRAKA, P., MEERSCHAERT, M.M., MCGOUGH, R.J. & ZHOU, Y. 2013 Fractional wave equations with attenuation. *Fract. Calc. Appl. Anal.* **16** (1), 262–272.
TAYLOR, G.I. 1950 The instability of liquid surfaces when accelerated in a direction perpendicular to their planes. I. *Proc. R. Soc. Lond. A: Math. Phys. Sci.* **201**(1065), 192–196.



https://doi.org/10.1017/jfm.2025.10265 Published online by Cambridge University Press

TERRONES, G. 2005 Fastest growing linear Rayleigh–Taylor modes at solid/fluid and solid/solid interfaces. *Phys. Rev. E* **71** (3), 036306.
UENO, K. 2003 Pattern formation in crystal growth under parabolic shear flow. *Phys. Rev. E* **68** (2), 021603.
UENO, K. 2004 Pattern formation in crystal growth under parabolic shear flow. II. *Phys. Rev. E* **69** (5), 051604.
UENO, K. 2007 Characteristics of the wavelength of ripples on icicles. *Phys. Fluids* **19** (9), 093602.
UENO, K. & FARZANEH, M. 2011 Linear stability analysis of ice growth under supercooled water film driven by a laminar airflow. *Phys. Fluids* **23** (4), 042103.
UENO, K., FARZANEH, M., YAMAGUCHI, S. & TSUJI, H. 2009 Numerical and experimental verification of a theoretical model of ripple formation in ice growth under supercooled water film flow. *Fluid Dyn. Res.* **42** (2), 025508.
WANG, Z., CALZAVARINI, E., SUN, C. & TOSCHI, F. 2021 How the growth of ice depends on the fluid dynamics underneath. *Proc. Natl Acad. Sci. USA* **118** (10), e2012870118.
WANG, Z., ZHANG, W., MAO, X., CHOI, K.-S. & LI, S. 2024 A consistent phase-field model for three-phase flows with cylindrical/spherical interfaces. *J. Comput. Phys.* **516**, 113297.
WATKINS, R.H., BASSIS, J.N. & THOULESS, M.D. 2021 Roughness of ice shelves is correlated with basal melt rates. *Geophys. Res. Lett.* **48** (21), e2021GL094743.
WEADY, S., TONG, J., ZIDOVSKA, A. & RISTROPH, L. 2022 Anomalous convective flows carve pinnacles and scallops in melting ice. *Phys. Rev. Lett.* **128** (4), 044502.
ZHANG, H., ZHANG, X., HE, F., LV, C. & HAO, P. 2022*a* How micropatterns affect the anti-icing performance of superhydrophobic surfaces. *Intl J. Heat Mass Transfer* **195**, 123196.
ZHANG, W., SHAHMARDI, A., CHOI, K.-S., TAMMISOLA, O., BRANDT, L. & MAO, X. 2022*b* A phase-field method for three-phase flows with icing. *J. Comput. Phys.* **458**, 111104.
ZWALLY, H.J., GIOVINETTO, M.B., LI, J., CORNEJO, H.G., BECKLEY, M.A., BRENNER, A.C., SABA, J.L. & YI, D. 2005 Mass changes of the Greenland and Antarctic ice sheets and shelves and contributions to sea-level rise: 1992–2002. *J. Glaciol.* **51** (175), 509–527.

https://doi.org/10.1017/jfm.2025.10265 Published online by Cambridge University Press